Article

Enhancing the Electrochemical Cycle Stability of Prussian-Blue Based Li-ion Storage Cathodes by the Incorporation of Ag and Ni Nanoparticles

Wen-Hsien Li * , Erdembayalag Batsaikhan , Ma-Hsuan Ma , Chun Chuen Yang

Posted Date: 16 August 2023

doi: 10.20944/preprints202308.1204.v1

Keywords: Rechargeable battery; Prussian Blue; Cathode material; Metallic nanoparticle; cyclability enhancement

Preprints (www.preprints.org) | NOT PEER-REVIEWED | Posted: 16 August 2023 doi:10.20944/preprints202308.1204.v1

Article

Enhancing the Electrochemical Cycle Stability of Prussian-Blue Based Li-ion Storage Cathodes by the Incorporation of Ag and Ni Nanoparticles

Wen-Hsien Li *, Erdembayalag Batsaikhan, Ma-Hsuan Ma and Chun Chuen Yang

Department of Physics, National Central University, Taoyuan 32001, Taiwan
* Correspondence: Correspondence: whli@phy.ncu.edu.tw; Tel.: +886-921-127692

Abstract: Taking advantage of fact that the surface electrons of metallic nanoparticles (NPs) can be effectively released even at a low voltage bias, we demonstrate an improvement in the electrochemical performance of nano-sized Prussian Blue (PB) based secondary batteries by the incorporation of bare Ag or Ni NPs onto the vicinity of the working PB NPs. It is found that the capacity for electrochemical energy storage of the 17-nm-PB-based battery is significantly higher than the capacity of 10-nm-PB-based, 35-nm-PB-based or 46-nm-PB-based batteries. There is a critical PB size for the highest electrochemical energy storage efficiency. The full specific capacity C_F of the 17-nm-PB-based battery stabilized to 62 mAh/g after 130 charge-discharge cycles at a working current of $I_W = 0.03$ mA. The addition of 14 mass-percent of Ag NPs in the vicinity of the PB NPs gives rise to a 32% increase in the stabilized C_F. A 42% increase in the stabilized C_F can be obtained with the addition of 14 mass-percent of Ag NPs on the working electrode of the 35-nm-PB-based battery. An enhancement of C_F is also found for electrodes incorporating bare Ni NPs but the effect is smaller.

Keywords: rechargeable battery; prussian Blue; cathode material; metallic nanoparticle; cyclability enhancement

1. Introduction

Although the Li-ion battery has become the most commonly used power source in portable electronic devices, efforts to enhance the cyclability of secondary batteries toward extending their cycle-life and increasing their energy-content continue [1-4]. It is the repeated extraction and restoration of electrochemical energy in the solid electrode that makes a battery reusable. The prerequisite for a solid compound to act as a cathode material for power storage is the existence of lattice sites from which ions can be extracted then reinserted after extraction [5-8]. Prussian Blue analogues (PBAs) with the general chemical formula $AM[M'(CN)_6]$ (A, alkali metal; M and M′, transition metal; hereafter denoted as A-MM′) [9,10] have been favored as promising active materials for cathodes [11-15]. The three-dimensional open channels in A-MM′s, enclosed by the MN_6-$M'C_6$-MN_6-$M'C_6$ octahedral chains along the three crystallographic directions, allow the migration of weakly bonded ions through the channels for energy extraction and restoration [16-23]. The voids for accommodating alkali ions in the open channels of the PBAs are uniformly distributed and spacious enough to receive ions as large as K^+. There are two possible redox active sites, M^{n+}-$M^{(n+1)+}$ and M'^{n+}-$M'^{(n+1)+}$, in A-MM′. Theoretically, when fully redox active, each site is capable of providing a specific capacity of 170.8 mAh/g during the charging-recharging cycle [24]. However, most PBAs give a specific capacity that is considerably smaller than 170.8 mAh/g [24], showing that only a portion of the metal ions are actually redox active. A high specific capacity, that can reach 140 mAh/g, has been reported in K-CuFe with a Li ion organic electrolyte, but the capacity decreases significantly with cycling due to the instability of the reduced state [16-19]. Stabilization of the reduced states by the application of a coating of stable K-NiFe onto high-capacity K-CuFe has been demonstrated to improve cycle stability [25]. It has been shown that the capacity of K-NiFe with organic electrolytes does not fade over 100 cycles [26,27]. Various approaches, such as employing nano-sized [27-29], core-shell [26-30], Ni-doped [31], polymer-coated [32-34] or carbon-coated [35] PBA, have been taken to improve cycle stability.

The accommodation of H_2O onto A sites and the replacement of $M'(CN)_6$ by $(H_2O)_6$ are unavoidable when the co-precipitation method is employed for synthesis. The intake of H_2O onto A sites reduces the number of sites available for A^+ restoration, while intake onto the M′ sites weakens the redox capability at the M′-C sites. These naturally occurring structural imperfections limit the redox capability of PBA as a cathode material. One way to provide additional electrons to facilitate redox activity in the PBAs is by the incorporation of metallic nanoparticles, where surface electrons are weakly bonded to the NPs. In this study, we demonstrate that the stability of the charging-discharging cycle can be greatly enhanced by the incorporation of capping-free Ag or Ni NPs into the vicinity of Na-FeFe NPs in the cathode compact.

2. Results and Discussion

2.1. Chemical composition

There are two lattice sites in the A-MM′ where H_2O can accommodate onto them during the co-precipitation reactions [36]. The M ions in A-MM′ form a face-centered cubic sublattice allowing the accommodation of either $M'(CN)_6$ or $(H_2O)_6$ between the two M ions, giving rise to a stoichiometric composition of $M[M'(CN)_6]_{1-y}[(H_2O)_6]_y$. The voids enclosed by the MN_6 and $M'C_6$ octahedra can accommodate either A ions or H_2O molecules or be left empty, giving a stoichiometric composition of $A_{2x}{\cdot}z(H_2O)$, with $2x + z \leq 1$. Taking A = Na, M = Fe, M′ = Fe and H_2O on the O sites in the present PB compounds, gives a constrained stoichiometric composition of $Na_{2x}Fe[Fe'(CN)_6]_{1-y}[(H_2O)_6]_y{\cdot}z(H_2O)$, with a charge balance of $2x + z \leq 1$ and $x + 2 - 3(1-y) = 0$ for diffraction pattern refinement. The diffraction patterns were analyzed using the General Structure Analysis System (GSAS) program [37], following the Rietveld profile refining method, assuming a cubic $Fm\bar{3}m$ symmetry. Figures 1A, 1B, 1C and 1D illustrate the observed (crosses) and calculated (solid lines) diffraction patterns of the Na-FeFe synthesized with reaction solutions of 25, 50, 70 and 85 °C, respectively. Giving a chemical composition of $Na_{0.38}Fe[Fe(CN)_6]_{0.82}[(H_2O)_6]_{0.18}{\cdot}0.34H_2O$ (marked $Na_{0.38}$-FeFe) for the Na-FeFe synthesized at 25 °C, a $Na_{0.41}Fe[Fe(CN)_6]_{0.84}[(H_2O)_6]_{0.16}{\cdot}0.36H_2O$ (marked $Na_{0.41}$-FeFe) for that synthesized at 50 °C, a $Na_{0.34}Fe[Fe(CN)_6]_{0.81}[(H_2O)_6]_{0.19}{\cdot}0.34H_2O$ (marked $Na_{0.34}$-FeFe) for that synthesized at 70 °C, and a $Na_{0.36}Fe[Fe(CN)_6]_{0.84}[(H_2O)_6]_{0.16}{\cdot}0.38H_2O$ (marked $Na_{0.36}$-FeFe) for that synthesized at 85 °C. Figure 2 illustrates the atomic arrangement of Na-FeFe, with 2/8 of the 8c sites and 1/9 of the 24e sites are occupied by H_2O. Occupations of H_2O onto the 8c or 24e sites will limit the redox capability during the electrochemical processes.

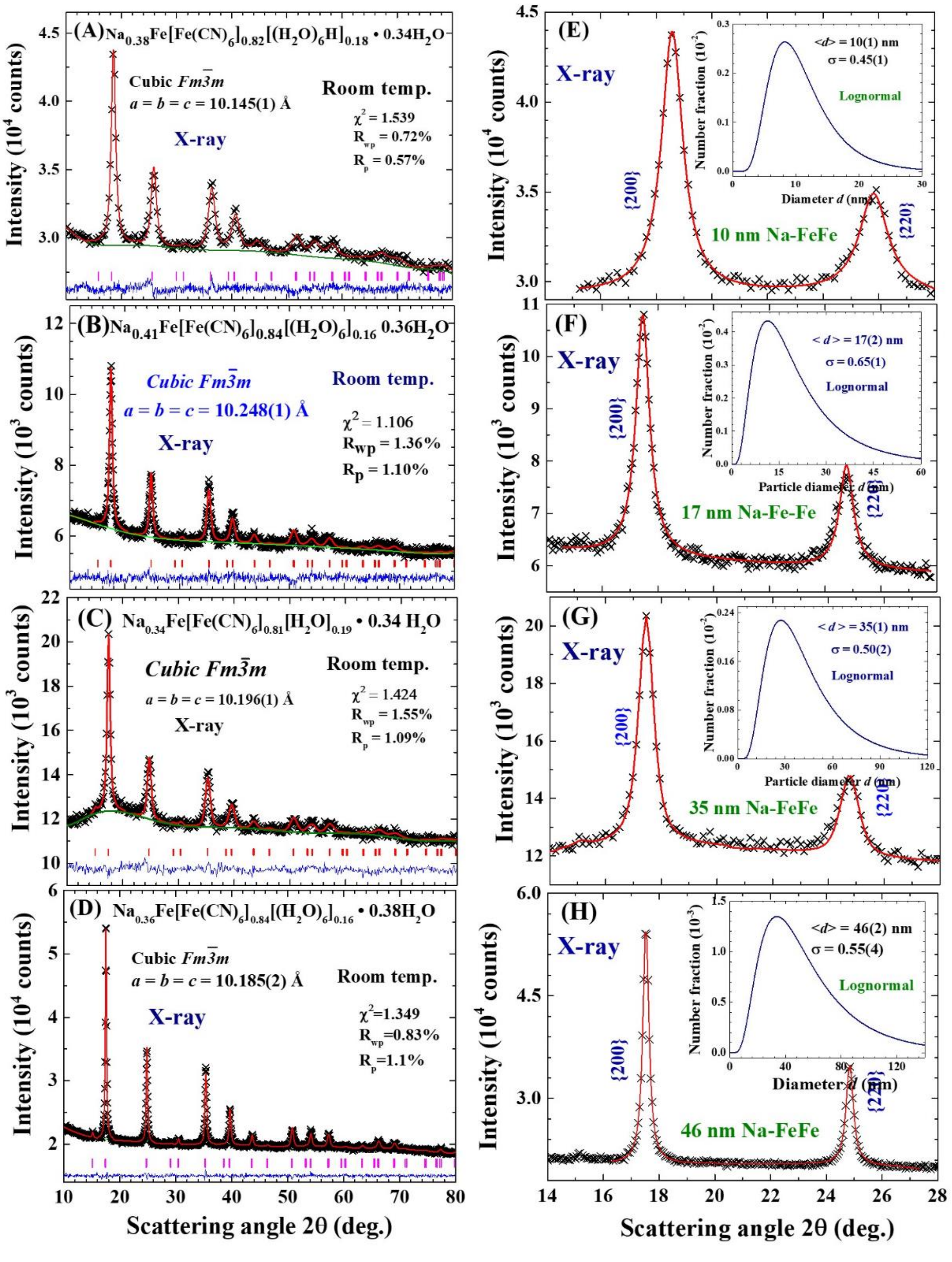

Figure 1. **(A)**-**(D)** The observed (crosses) and calculated (solid lines) x-ray diffraction patterns of the Na-FeFe synthesized with reaction solutions at **(A)** 25 °C, **(B)** 50 °C, **(C)** 70 °C and **(D)** 85 °C, assuming a cubic $Fm\bar{3}m$ symmetry for the crystalline structure, giving a chemical composition of $Na_{0.38}Fe[Fe(CN)_6]_{0.82}[(H_2O)_6]_{0.18}{\cdot}0.34H_2O$ for **(A)**, $Na_{0.41}Fe[Fe(CN)_6]_{0.84}[(H_2O)_6]_{0.16}{\cdot}0.36H_2O$ for **(B)**, $Na_{0.34}Fe[Fe(CN)_6]_{0.81}[(H_2O)_6]_{0.19}{\cdot}0.34H_2O$ for **(C)**, and $Na_{0.36}Fe[Fe(CN)_6]_{0.84}[(H_2O)_6]_{0.16}{\cdot}0.38H_2O$ for **(D)**. The differences between the calculated and observed patterns are plotted at the bottom. The solid vertical lines mark the calculated positions of the Bragg reflections of the proposed crystalline structure. **(E)-(H)** The observed (crosses) and calculated (solid lines) {200}+{220} peak profiles of the Na-FeFe synthesized with reaction solutions at **(E)** 25 °C, **(F)** 50 °C, **(G)** 70 °C and **(H)** 85 °C, assuming a lognormal size distribution, given a mean particle diameter of d = 10(1) nm with a standard deviation width of σ = 0.45(1) for **(E)**, d = 17(2) nm with σ = 0.65(1) for **(F)** d = 35(1) nm with σ = 0.50(2) for **(G)**, and d = 46(2) nm with σ = 0.55(4) for **(H)**. The insets show the size distributions obtained from the fits.

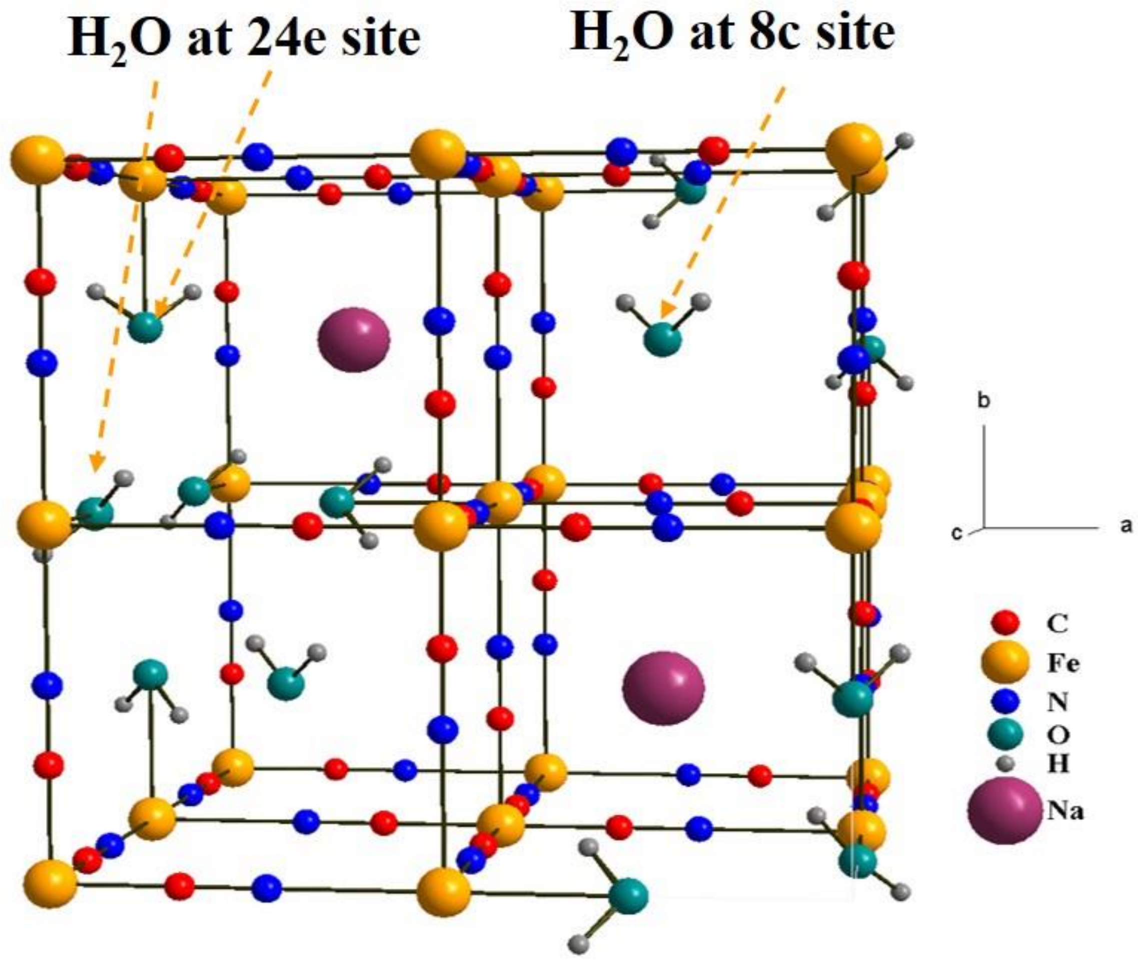

Figure 2. Schematic drawing of the crystalline structure of the Na-FeFe, with 2/8 of the 8c sites and 1/9 of the 24e sites occupied by H_2O. This structure of PB can be viewed, when there is no atomic deficiency, as consisting of Fe-N-C-Fe-C-N-Fe chains along the three crystallographic axis directions.

2.2. Particle size

The x-ray diffraction peaks of $Na_{0.38}$-FeFe are significantly broader in width than those of $Na_{0.36}$-FeFe (Figures 1A and 1B), revealing the particles in the $Na_{0.38}$-FeFe NP assembly are much smaller than those in the $Na_{0.36}$-FeFe assembly. In addition, the x-ray diffraction peaks of the four Na-FeFe, Ag and Ni NP assemblies appear to be much broader than the instrumental resolution, reflecting the broadening of the peak profiles due to the finite-size effect. The size distributions and mean particle diameters of the NP assemblies were determined by fitting the diffraction peaks to the diffraction profiles of finite sized particles. Taking a Lorentzian diffraction profile of the peak width $w_i(d_i)$ from each nanoparticle of diameter d_i, the diffraction intensity I_{hkl} of the (hkl) Bragg reflection at a scattering angle 2θ from a multi-dispersed NP assembly having a log-normal size distribution $n_i(d_i)$ takes the form of [37, 38]

$$I_{hkl}(2\theta, w_i, n_i) = \mathrm{C}\sum_{d_i}\left(\frac{2}{\pi}\right)\left[\frac{w_i}{4(2\theta-2\theta_{hkl})^2+w_i^2}\right]n_i(d_i) \qquad (1)$$

$$with\; w_i(d_i) = \frac{0.94\lambda}{d_i\cos\theta_{hkl}}$$

$$and\; n_i(d_i) = \frac{1}{d_i\sqrt{2\pi}\sigma}exp\left\{-\frac{(lnd_i - lnd_m)^2}{2\sigma^2}\right\},$$

where C is the instrumental scale factor, $2\theta_{hkl}$ is the Bragg position of the (*hkl*) reflection, λ is the x-ray wavelength, d_m is the mean particle diameter and σ is the standard deviation of the size distribution of the NP assembly. Figures 1E, 1F, 1G and 1H show the observed (crosses) and calculated (solid lines) {200} and {220} diffraction peak profiles of the $Na_{0.38}$-FeFe, $Na_{0.41}$-FeFe, $Na_{0.34}$-FeFe and $Na_{0.36}$-FeFe NP assemblies, respectively, obtained from the fits of the diffraction profiles to the expression (1). A mean particle diameter of d = 10(1) nm with a deviation width of σ = 0.45(1) was obtained for the $Na_{0.38}$-FeFe NP assembly (inset to Figure 1E), d = 17(2) nm with σ = 0.65(1) for the $Na_{0.41}$-FeFe NP assembly (inset to Figure 1F), d = 35(2) nm with σ = 0.50(2) for the $Na_{0.34}$-FeFe NP assembly (inset to Figure 1G) and d = 46(2) nm with σ = 0.55(4) for the $Na_{0.36}$-FeFe NP assembly (inset to Figure 1H). It appears that larger particles were obtained for the Na-FeFe synthesized at a higher reaction temperature. Profile analysis of the x-ray diffraction peaks of the Ag and Ni NP assemblies give d = 7.6(3) nm with σ = 0.65(8) for the Ag NP assembly (Figure 3A) and d = 12.4(3) nm with σ = 0.51(7) for the Ni NP assembly (Figure 3B). The reaction temperature, chemical composition, lattice parameters, mean particle diameter, and deviation width of the size distribution for each of the four Na-FeFe compounds, the Ag NP, and the Ni NP assemblies are listed in Table 1.

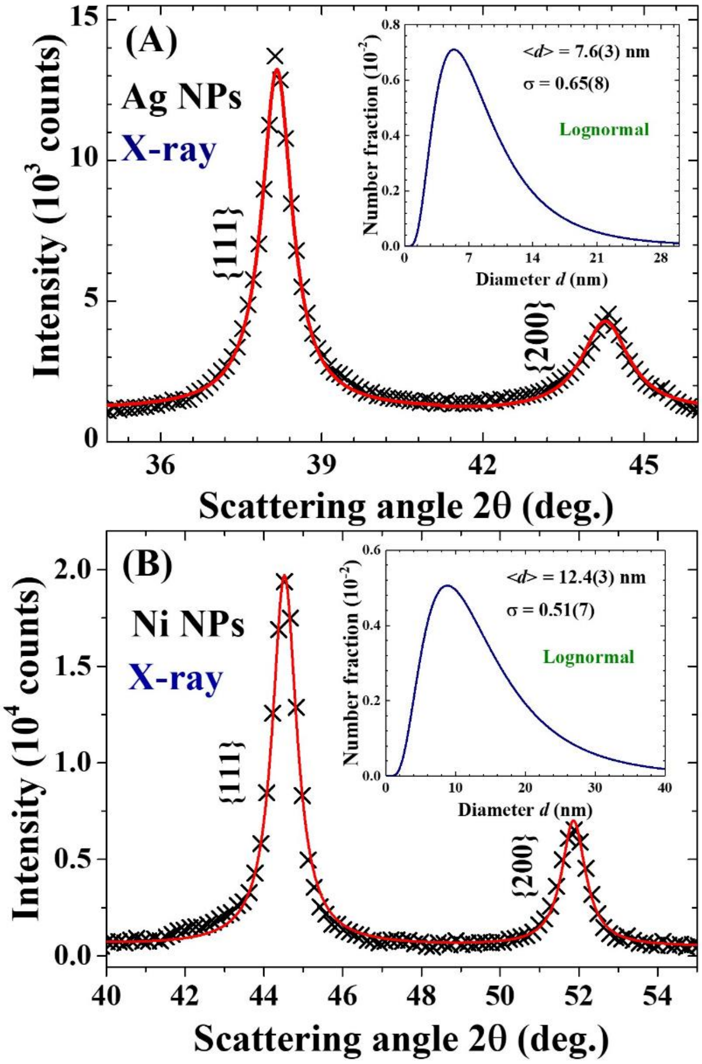

Figure 3. The {111}+{200} peak profiles of the **(A)** Ag and **(B)** Ni NP assemblies obtained at room temperature. The solid lines indicate the calculated diffraction profiles, assuming a lognormal size distribution, as shown in the insets, revealing mean particle diameters of 7.6(3) nm for the Ag NP assembly and 12.4(3) nm for the Ni NP assembly. The insets show the size distributions obtained from the fits.

Table 1. Labels, reaction solution temperatures, chemical compositions, lattice parameters, mean particle diameters, and deviation widths of the size distributions of the four Na-FeFe compounds used in this study.

Label	T (°C)	Chemical composition	*a* (Å)	*d* (nm)	σ
$Na_{0.38}$-FeFe	25	$Na_{0.38}Fe[Fe(CN)_6]_{0.82}[(H_2O)_6]_{0.18}\cdot 0.34H_2O$	10.145(1)	10(1)	0.45(2)
$Na_{0.41}$-FeFe	50	$Na_{0.41}Fe[Fe(CN)_6]_{0.84}[(H_2O)_6]_{0.16}\cdot 0.36H_2O$	10.248(1)	17(2)	0.65(1)
$Na_{0.34}$-FeFe	70	$Na_{0.34}Fe[Fe(CN)_6]_{0.81}[(H_2O)_6]_{0.19}\cdot 0.34H_2O$	10.196(1)	35(2)	0.50(2)
$Na_{0.36}$-FeFe	85	$Na_{0.36}Fe[Fe(CN)_6]_{0.84}[(H_2O)_6]_{0.16}\cdot 0.38H_2O$	10.185(2)	46(2)	0.55(4)
Ag		Ag	4.088(1)	7.6(3)	0.65(8)
Ni		Ni	3.526(3)	12.4(3)	0.51(7)

T = temperature of the reaction solution
a = lattice constant at room temperature
d = mean particle diameter
σ = deviation width of size distribution of the nanoparticle assembly

2.3. *Ultimate size for energy storage*

The galvanostatic charge-discharge (GCD) cycles were performed in constant working current I_W mode for each cycle. The working electrodes packed using 10, 17, 35 and 46 nm Na-FeFe are labelled 10NFF, 17NFF, 35NFF and 46NFF, respectively. Obvious differences in the GCD profiles are observed for the batteries using different sizes of Na-FeFe in the working electrode. The GCD profiles of the 17NFF battery take the longest in time to complete a cycle, followed by the 35NFF battery, then the 46NFF battery, but the 10NFF battery takes the shortest time (Figure 4A). Among the four batteries studied, the 17NFF battery had the highest energy capacity. The full specific capacity (FSC) C_F of 17NFF battery reached 86 mAh/g in the initial cycle at I_W = 0.015 mA, but it gradually decayed to 76 mAh/g and then stabilized after 40 GCD cycles (open triangles in Figure 4B). A relatively low C_F of 42 mAh/g, which is only 50% that of 17NFF, was obtained for the 10NFF battery (open stars in Figure 4B). The decay profiles of C_F with respect to the number of GCD cycles completed for the four batteries are similar. The Na and H_2O contents in the four Na-FeFe compounds studied are similar (Table 1). It is mainly the size of Na-FeFe that gives rise to the differences in the GCD behavior. Apparently, there is a size limit to the Na-FeFe NPs for the highest electrochemical energy storage efficiency. The higher energy storage efficiency of the 17NFF battery compared to the 35NFF and 46NFF batteries is a direct result of there being more Na-FeFe particles for dispersal in the working electrode allowing for the receive and release of Li^+ ions. On the other hand, the Li^+ ions are received and releases at the surfaces of the Na-FeFe NPs facing the anode. The reduction in energy storage efficiency of the 10NFF battery is thus a result of the appearance of a large amount of surface atoms that cannot effectively store Li^+ ions. It is the competition between the number of NPs that are available for dispersal over the electrode and the loss of storage capability for the atoms on the surfaces of the NPs that result in the ultimate size limit for electrochemical energy storage by the Na-FeFe NPs.

doi:10.20944/preprints202308.1204.v1

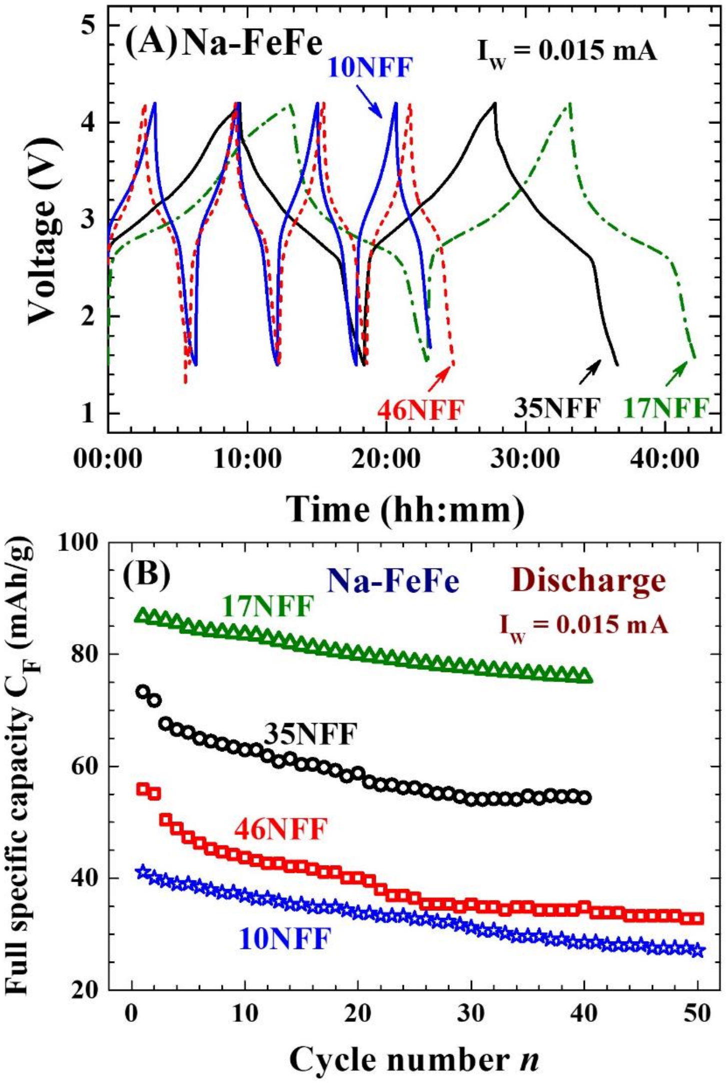

Figure 4. (A) Comparison of charge-discharge profiles of the 17NFF (dotted dashed lines), 35NFF (black solid lines), 46NFF (dashed lines) and 10NFF (blue solid lines) batteries. The 17NFF battery takes the longest time to complete a cycle, whereas the 10NFF takes the shortest. **(B)** Direct comparisons between the decay profiles $C_F(n)$ of the 17NFF (open triangles), 35NFF (open circles), 46NFF (open squares) and 10NFF (open stars) batteries at I_W = 0.015 mA. All four batteries have similar decay profiles $C_F(n)$.

The full specific capacity C_F can be affected by the working current employed in running the GCD cycles. The C_F of the two 35NFF batteries, configured using working electrodes with the same set of coatings, were measured employing a sequence of different I_W for the GCD cycles (Figure 5). A C_F of 84 mAh/g was obtained for the two 35NFF batteries at I_W = 0.015 mA. A direct drop in C_F appeared whenever the I_W was raised. The C_F dropped to 60 mAh/g after runs through a series of changes in the I_W from 0.015 to 0.03 to 0.06 to 0.09 mA. Remarkably, C_F jumped back to 78 mAh/g when the I_W was subsequently reduced to 0.015 mA. The behavior of C_F with respect to the I_W shows that the loss of C_F at a high I_W is linked to the reduced efficiency in receiving Li^+ onto the Na-FeFe. Discharging at a high I_W drives the accumulation of more Li^+ ions onto the cathode plate rather than entering the Na-FeFe NPs for energy storage, which builds the potential between the cathode and the anode, but with fewer Li+ ions stored in the Na-FeFe NPs.

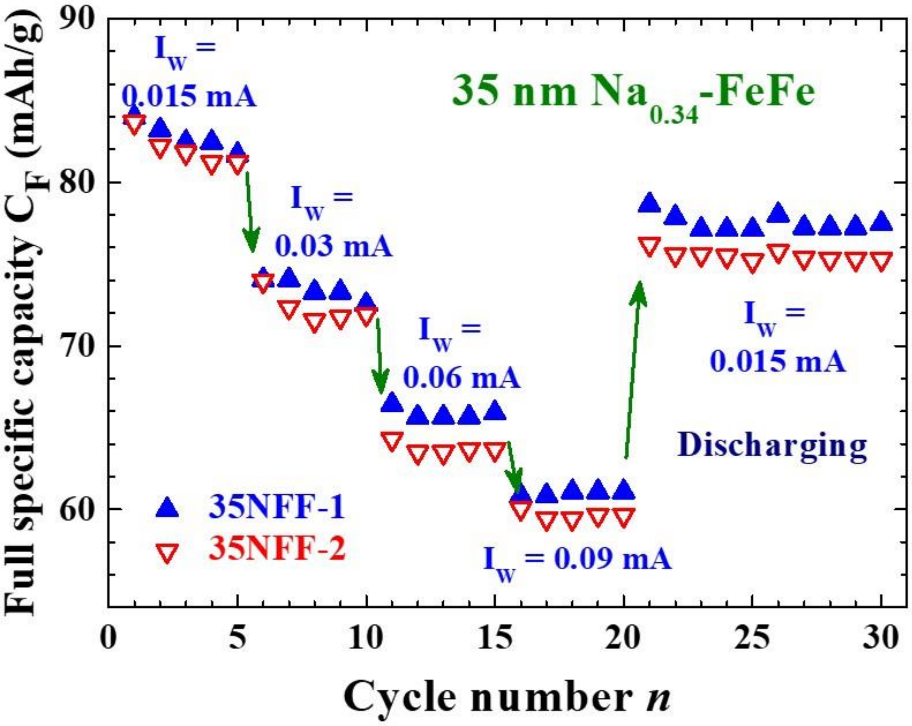

Figure 5. Variations of full specific capacity C_F on the working current I_W employed in the charge-discharge cycles. The C_F drops from 86 to 60 mAh/g as the I_W increases from 0.015 to 0.03 to 0.06 to 0.09 mA, but jumps back to 78 mAh/g once the working current is subsequently reduced to 0.015 mA.

2.4. Enhanced electrochemical stability

The amount of Ag/Ni NPs added into the electrode is specified in the label for each battery. For example, the label 17NFF+14%Ag indicates a 17NFF battery with an addition of 14 mass percent of Ag NPs onto the working electrode. In the initial stage, represented by the 2nd GCD cycle, the 35NFF+14%Ni battery took 10% longer to complete a GCD cycle than did its counterpart battery 35NFF (dashed lines in Figure 6A). The difference in the time taken to complete a GCD cycle increased to 15% after the completion of 200 GCD cycles (solid lines in Figure 6A). The Coulomb efficiency of nearly 100% obtained for the 2nd GCD cycle was retained after 200 GCD cycles. It appears that the incorporation of Ni NPs onto the working electrode can enhance as well as stabilize the energy capacity stored in the battery.

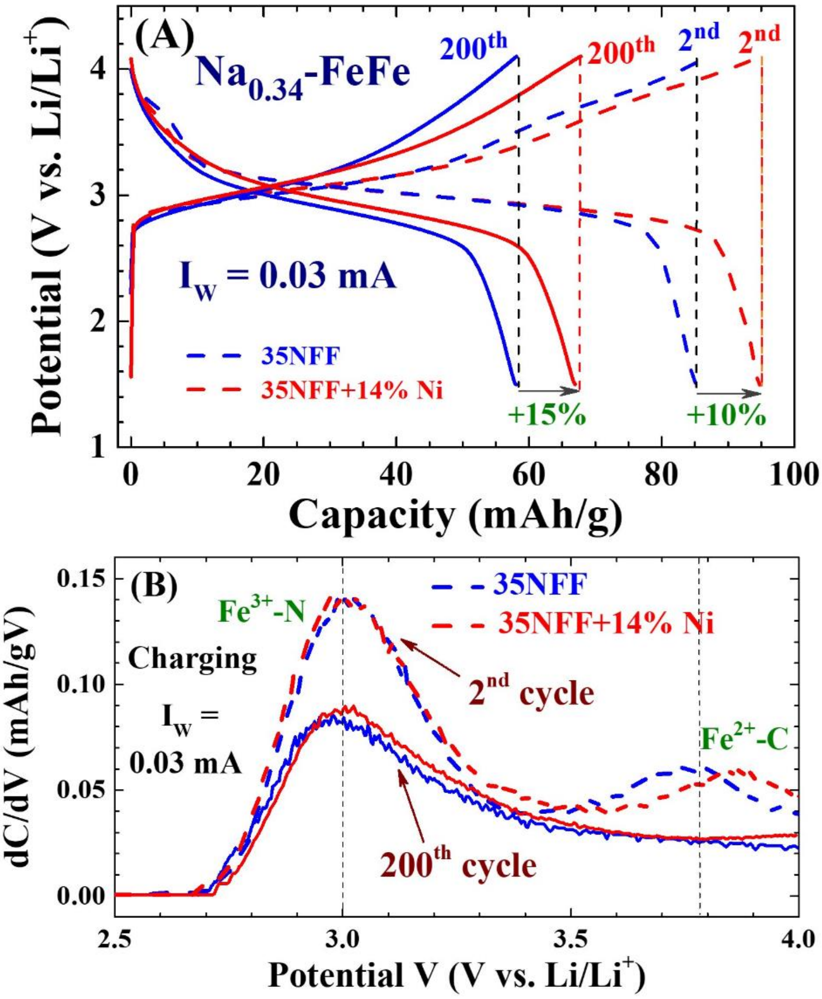

Figure 6. (A) Direct comparison between the charge-discharge profiles of the 35NFF and 35NFF+14%Ni batteries in the 2nd (dashed lines) and 200th (solid lines) GCD cycles. Differences in the full specific capacity C_F between the two batteries increase from 10% in the 2nd cycle to 15% in the 200th cycle. **(B)** Variations of differential capacity dC/dV with potential V of the 35NFF and 35NFF+14%Ni batteries in the 2nd (dashed lines) and 200th (solid lines) GCD cycles. The two separated peaks clearly reveal both the Fe^{2+}-C and the Fe^{3+}-N sites do participate in redox reactions.

Two separated peaks are clearly revealed in the dC/dV curves for the initial GCD cycles (dashed lines in Figure 6B). The one at around 3.0 V is from the redox reaction at the Fe^{3+}-N sites, whereas the one at around 3.8 V is from reaction at the Fe^{2+}-C sites. The lower redox efficiency for the Fe^{2+}-C sites reflects a reduction in the redox activity because of the partial occupation of the sites by H_2O. The main difference between the dC/dV curves of the 35NFF and 35NFF+14%Ni batteries in the initial stage (dashed lines in Figure 6B), which appears in the high voltage regime, shows that the incorporation of Ni NPs facilitates the redox reactions more on the Fe^{2+}-C sites than on the Fe^{3+}-N sites. As expected, there is a reduction in the redox efficiency at both the Fe^{2+}-C and Fe^{3+}-N sites after 200 GCD cycles, but at a noticeable smaller rate for the 35NFF+14%Ni battery than for the 35NFF battery. The incorporation of Ni NPs in the vicinity of $Na_{0.24}$-FeFe NPs enhances the GCD cycle stability. This behavior may be understood as arising from the participation of loosely bounded surface electrons of the Ni NPs in the redox reactions with Li^+ ions during GCD cycles.

In the initial stage, the full specific capacity C_F of the 35NFF+14%Ni battery reached 95 mAh/g, which is 10% higher than the 86 mAh/g of the 35NFF battery (Figure 7A). The C_F of both batteries stabilized after 200 GCD cycles. C_F of the 35NFF+14%Ni battery reduced to 67 mAh/g, but this was still 15% higher than the 58 mAh/g of the 35NFF battery. The profiles of the decay of C_F with respect to the number *n* of GCD cycles completed of the 35NFF+14%Ni and 35NFF batteries are similar. An enhancement in the capacity is also seen in the batteries with Ag NPs incorporated in the working electrodes. The amount of Ag NPs added to the working electrodes significantly affects the enhancement factor and the decay profile of $C_F(n)$ (Figure 7B). The incorporation of 14% Ag NPs enhances the C_F by 30%, with the initial C_F reaching 110 mAh/g and stabilizing at 78 mAh/g after 30 GCD cycles (open circles and squares in Figure 7B). On the other hand, the $C_F(n)$ remains stable for batteries incorporating 25% or 35% Ag NPs onto the working electrode, with the C_F remaining around 78 mAh/g (open stars and triangles in Figure 7B). The C_F of the three 35NFF+14%Ag, 35NFF+25%Ag and 35NFF+35%Ag batteries stabilized to 78 mAh/g, 44% higher than the 55 mAh/g of the 35NFF battery.

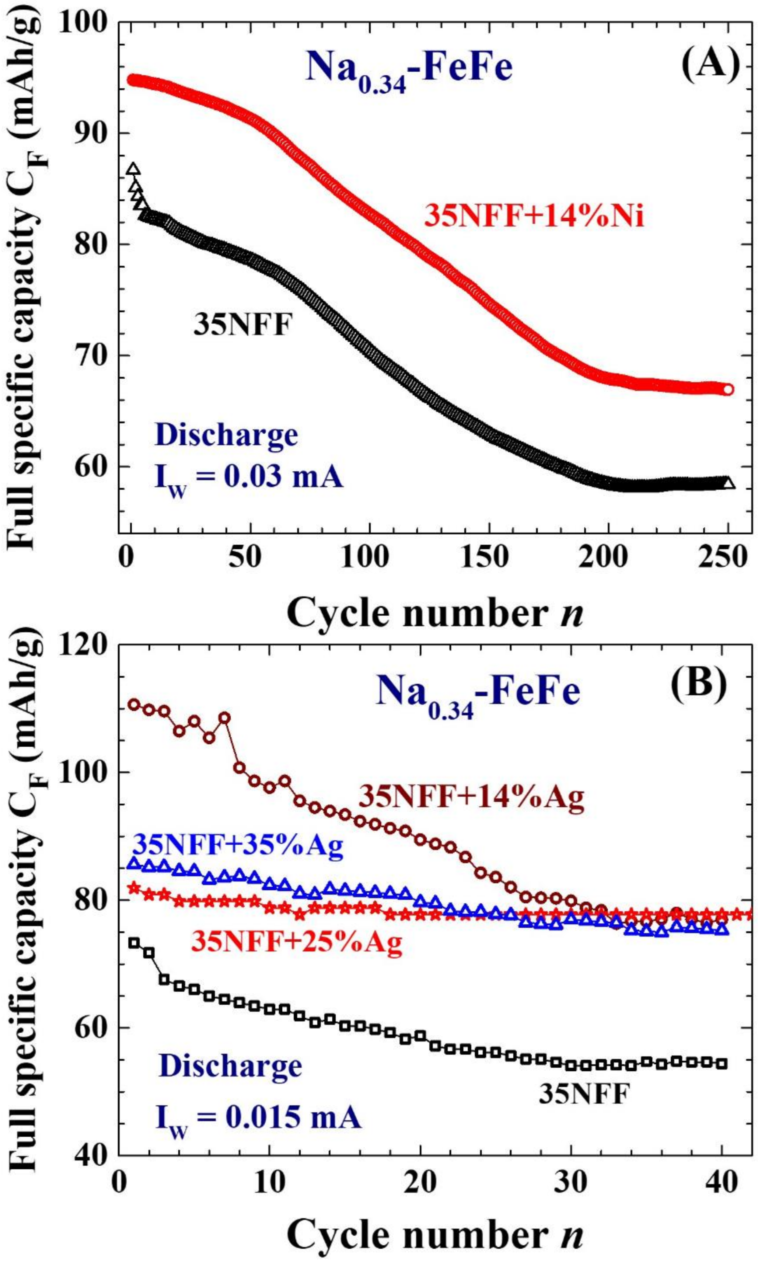

Figure 7. (A) Direct comparison between the decay profiles $C_F(n)$ of the 35NFF (open triangles) and 35NFF+14%Ni (open circles) batteries. **(B)** Direct comparison between the decay profiles $C_F(n)$ of the 35NFF (open squares), 35NFF+14%Ag (open circles), 35NFF+25%Ag (open stars) and 35NFF+35%Ag (open triangles) batteries.

The decay rate of $C_F(n)$ is largely reduced when Ag or Ni NPs are added into the working electrodes of the 17 nm $Na_{0.41}$-FeFe batteries. The $C_F(n)$ of the 17NFF battery decayed by 30% (from 88 to 62 mAh/g) before stabilizing after 130 GCD cycles (open squares in Figure 8A). The addition of

14% Ni NPs reduced the decay in $C_F(n)$ to 16% (from 88 to 74 mAh/g) (open triangles and stars in Figure 8A); whereas the addition of 14% Ag NPs reduced the decay in $C_F(n)$ to 7% (from 88 to 82 mAh/g) (open circles in Figure 8A). The higher efficiency in stabilization of C_F for the 7.6 nm Ag NPs than for the 12.4 nm Ni NPs arises from there being more surface electrons available for redox reactions of Li^+ ions in the Ag NPs than in the Ni NPs.

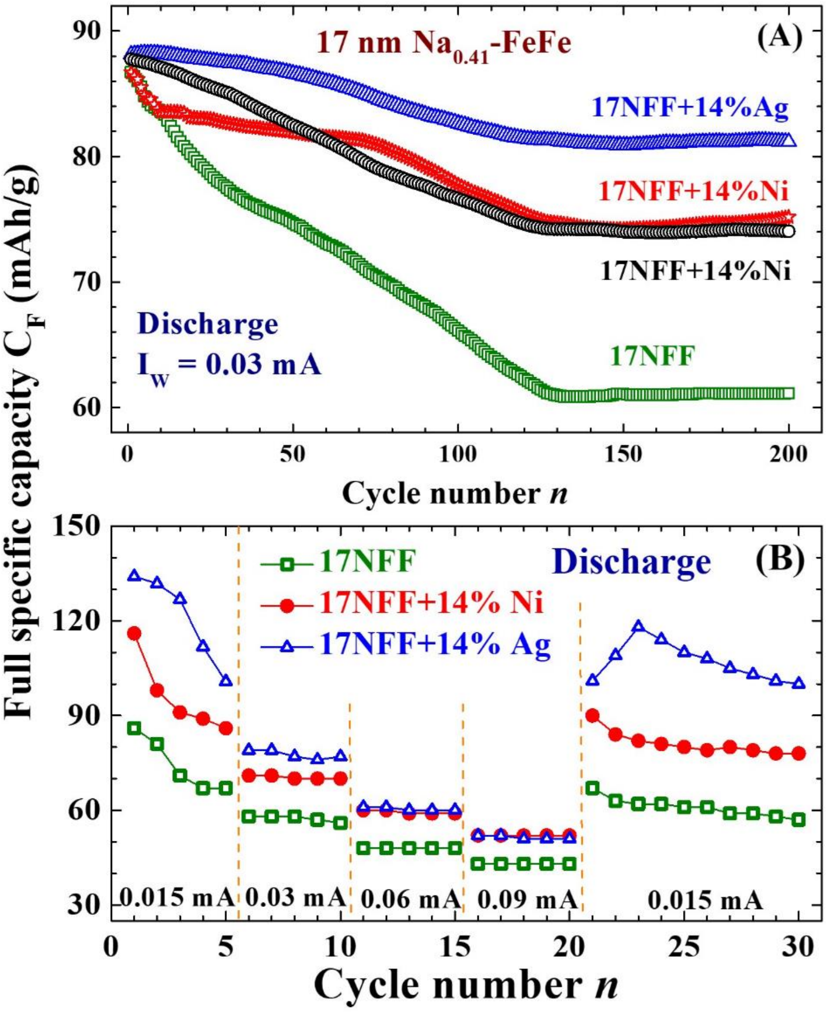

Figure 8. (A) Direct comparison between the decay profiles $C_F(n)$ of the 17NFF (open squares), 17NFF+14%Ni (open circles and stars) and 17NFF+14%Ag (open triangles) batteries. **(B)**Variation of the full specific capacity C_F with the number n of GCD cyclse completed, revealing a sudden drop in the C_F once the working current I_W is increased, but a jump back to a higher C_F once I_W is subsequently reduced.

A lower working current gives rise to a higher energy storage rate is also seen in the 17 nm $Na_{0.41}$-FeFe batteries with and without the addition of Ag/Ni NPs onto the working electrodes. A higher C_F for the 17NFF+14%Ag than for the 17NFF+14%Ni than for the 17NFF is revealed regardless of the I_W employed (Figure 8B). The C_F of the 17NFF+14%Ag battery stabilized from 88 to 81 mAh/g after 130 GCD cycles when I_W = 0.03 mA was employed from the initial cycle (open circles in Figure 8A). On the other hand, it was reduced from 135 to 101 mAh/g after 5 GCD cycles with I_W = 0.015 mA, but then dropped directly to 79 mAh/g once the I_W was raised to 0.03 mA at the 6th GCD cycle, then further dropped to 61 and 52 mAh/g at I_W = 0.06 and 0.09 mA, respectively (open triangles in Figure 8B). The C_F jumped back to 101 mAh/g once the I_W was again reduced to 0.015 mA. This behavior of a lower I_W which gives rise to a higher C_F with a larger decay in C_F was also observed in the 17NFF+14%Ni and 17NFF batteries (filled circles and open squares in Figure 8B).

3. Materials and methods

3.1. Synthesis of Prussian Blue nanoparticles

Four sets of Na-FeFe NPs were synthesized by the co-precipitation method. All reagents were purchased from Alfa-Aesar, Acros-Organics or Nihon-Shiyaku and used without further purification. The deionized water used in the synthetic procedures was obtained from a Milli-Q-Gard purification system. Fast PES Bottle Top Filters with a 0.45 μm pore size obtained from Nalgene were used during the synthesis process. Two separate solutions of 0.1M $Na_4Fe(CN)_6$ and 0.1M $FeCl_3$ were simultaneously dropped at a rate of 5 sec/drop into deionized water maintained at a temperature of 25, 50, 70 or 85 °C, as illustrated in Figure 9. Each solution was slowly stirred at 200 rpm for another 24 hours after the addition of the reaction solution was completed. The microcrystalline powder was isolated from the solution by centrifugation before being washed and re-dispersed in 100 ml of deionized water. This washing process was repeated for three times before the wet-muddy powder was dried at 95 °C in a vacuum for 24 hrs.

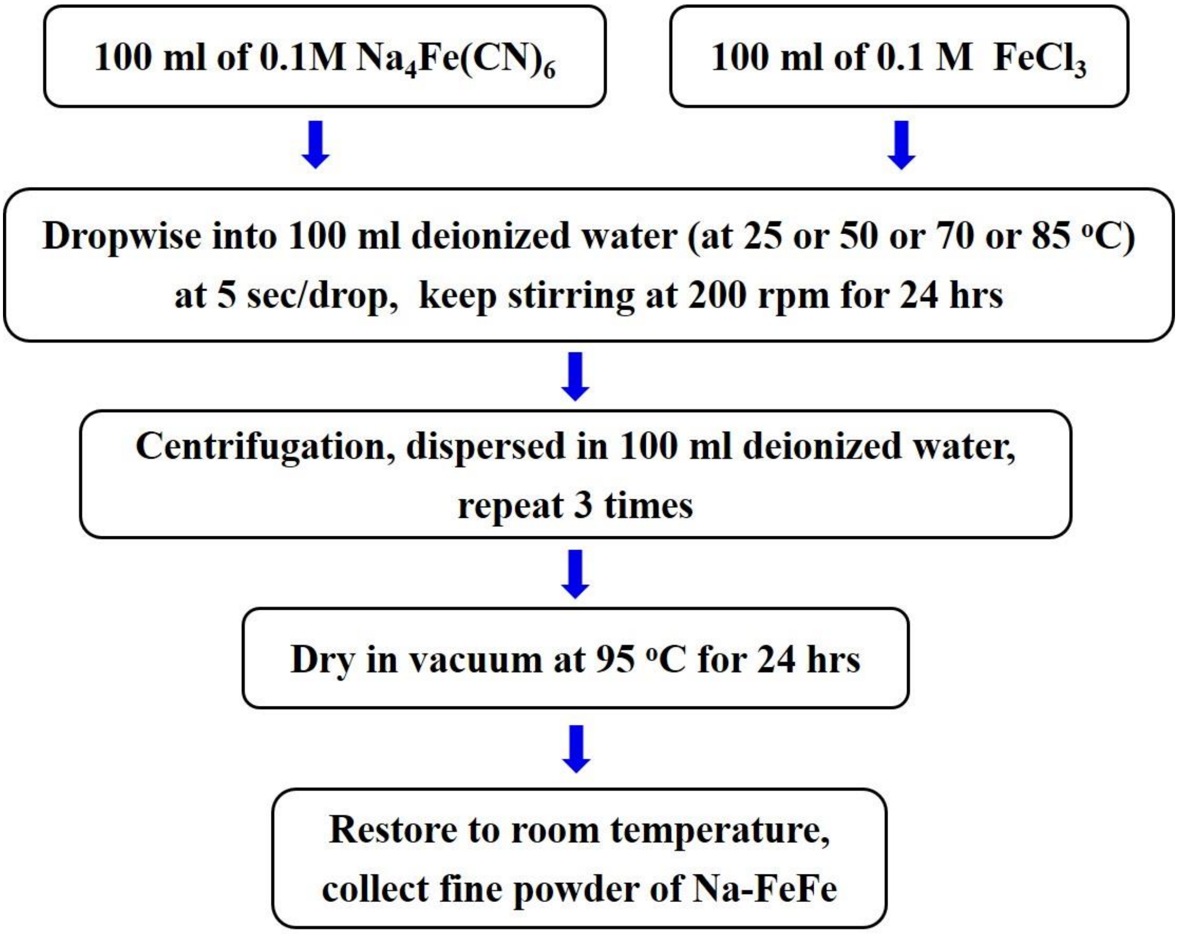

Figure 9. Process for the fabrication of Na-FeFe nanoparticles, followed the co-precipitation method. The four sets of Na-FeFe nanoparticles were synthesized separately with the reaction solution maintained at temperatures of 25, 50, 70 or 85 °C.

3.2. Synthesis of Ag and Ni nanoparticles

The Ag/Ni NPs were fabricated by employing the gas condensation method [38]. High-purity Ag/Ni ingots (0.6 g, 99.99% pure, ~2 mm in diameter) were heated by a current source of 65/50 A and were evaporated at a rate of 0.05 Å/s in an Ar atmosphere of 1.5 torr. The evaporated particles were collected on a non-magnetic SS316 stainless steel plate placed 20 cm above the evaporation source, maintained at 77 K. After natural cooling to room temperature, the NPs, which were only loosely attached to the collector, were stripped off in a N_2 atmosphere. The samples thus fabricated were in powdered form, consisting of macroscopic amounts of individual Ag/Ni NPs.

3.3. X-ray diffraction

doi:10.20944/preprints202308.1204.v1

The X-ray diffraction measurements were performed on a Bruker D8 ADVANCE diffractometer, employing the reflection geometry with an incident wavelength of $\lambda = 1.5406$ Å from a Cu target and collimation slits of 0.3 mm in width before and after the sample position. For each measurement, ~0.1 g of the sample was sharped into a width of ~1 mm to receive the whole of the x-ray beam at all scattering angle.

3.4. Electrochemical experiments

Electrochemical tests were conducted using a CR2032 coin-cell configuration assembled in a N_2 atmosphere with H_2O and O_2 levels both below 0.01 ppm. The circular working electrode (coated onto thin aluminum foil 0.02 mm thick) for Li-ion insertion and extraction contained a uniformly mixed Na-FeFe : Ag/Ni NPs (if applicable) : acetylene-black (AB) : polyvinylidene-fluoride (PVDF) : N-Methyl-pyrrolidone (NMP) slurry (dried in a vacuum at 120 $^{\circ}$C for 24 hrs) with mass ratios of 7 : 1 (14%), 1.75 (25%) or 2.45 (35%) : 2 : 1 : 40. Details of the electrode fabrication processes are shown in Figure 10. The mass loading for the electrode is 1.9 mg of Na-FeFe over the circular working area which was 15 mm in diameter and 0.1 mm thick (17.67 mm^3 in volume). A piece of porous polypropylene (1.8 mm thick) was used as a separator between the Na-FeFe containing working electrode and lithium metal electrode, which was filled with 1 M of $LiPF_6$ dissolved in mixed ethylene carbonate (EC) and diethyl carbonate (DEC) solutions (1 : 1 v/v %) as the electrolyte. The charge-discharge experiments were performed with a HOKUTO HJSD8 in constant current mode, with a cut-off voltage of 1.5 V for Li-ion insertion and 4.0 V for Li-ion extraction. All capacities are expressed per gram of PB.

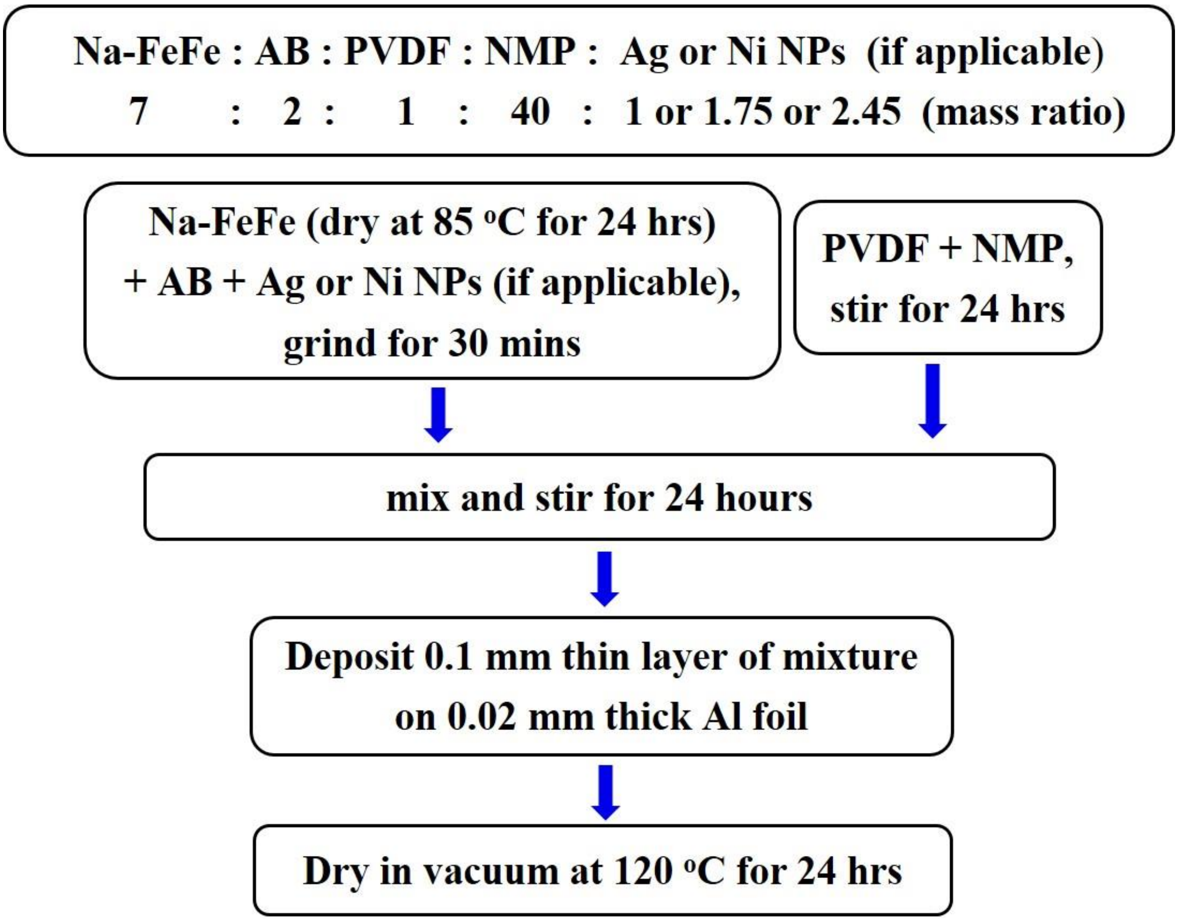

Figure 10. Procedure for the preparation of the working electrode containing Na-FeFe NPs, where AB represents acetylene-black, PVDF the polyvinylidene-fluoride, and NMP the N-Methyl-pyrrolidone. Mass ratios of 7 : 1, 7 : 1.75 or 7 : 2.45 were used for the Na-FeFe : Ag/Ni NPs amounts to a mass ratio of 14%, 25% or 35% of Ag/Ni NPs in the electrode

4. Conclusions

Prussian Blue with a general chemical formula of $Na_xFe[Fe'(CN)_6]_{1-y}[(H_2O)_6]_y{\cdot}z(H_2O)$ is demonstrated to be an active cathode material for the electrochemical energy storage. Four sets of Prussian Blue NPs, with mean particle diameters of 11, 17, 35 and 46 nm, were fabricated by co-precipitation of $Na_4Fe(CN)_6$ and $FeCl_3$ in deionized water each at a selective temperature. Among these, the 17 nm Na-FeFe NPs had the highest efficiency in terms of electrochemical energy storage when used as the working electrode of a rechargeable battery. There are two redox active Fe^{2+}-C and Fe^{3+}-N sites in Na-FeFe. The unavoidable replacement of $Fe(CN)_6$ by $(H_2O)_6$ during the co-precipitation in deionized water limits the redox activity of Na-FeFe when used as a working electrode. We demonstrate that the introduction of bare Ag or Ni NPs in the vicinity of the working Na-FeFe NPs can effectively stabilize the GCD cycles. In particular, the addition of 14 mass percent of 7.6 nm Ag NPs to the vicinity of the 17 nm Na-FeFe NPs could enhance the storage capacity by as much as 32%, and the addition of 14 mass percent of 12.4 nm Ni NPs led to an enhancement in storage capacity of 24%. The storage capacity of Na-FeFe NPs was enhanced by the participation in redox reactions of the weakly bonded surface electrons of the Ag/Ni NPs. It is hence essential to use capping free metallic NPs for effective enhancement.

Author Contributions: W.H.L. and E.B. designed the study; E.B. and M.H.M. synthesized the sample; E.B., M.H.M. and C.C.Y. performed the measurements; E.B., M.H.M., C.C.Y., and W.H.L. analyze all data; all of the authors discussed the results; W.H.L. wrote the manuscript with discussion and input from all of the authors. All authors have read and agreed to the published version of the manuscript.

Funding: This work was supported by the Ministry of Science and Technology of Taiwan under Grant No. MOST 110-2112-M-008-034.

Conflicts of Interest: The authors declare no conflict of interest.

References

1. Etacheri, V.; Marom, R.; Elazari, R.; Salitra, G.; Aurbach, D. Challenges in the development of advanced Li-ion batteries: a review. *Energy Environ. Sci.* **2011**, *4*, 3243-3262.
2. Goodenough, J.B.; Park, K.S. The Li-ion rechargeable battery: a perspective. *J. Am. Chem. Soc.*, **2013**, *135*, 1167-1176.
3. Choi, J.W.; Aurbach, D. Promise and reality of post-lithium-ion batteries with high energy densities. *Nat. Rev. Mater*. **2016**, *1*, 1-16.
4. Kim, T., Song, W.; Son, D.Y.; Ono, L.K.; Qi, Y. Lithium-ion batteries: outlook on present, future, and hybridized technologies. *J. Mater. Chem. A* **2019**, *7*, 2942-2964.
5. Liu, C.; Neale, Z.G.; Cao, G. Understanding electrochemical potentials of cathode materials in rechargeable batteries. *Mater. Today* **2016**, *19*, 109-123.
6. Dong, C.; Gao, W.; Jin, B.; Jiang, Q. Advances in cathode materials for high-performance lithium-sulfur batteries. *iScience* **2018**, *6*, 151-198.
7. Liu, Z.; Yuan, X.; Zhang, S.; Wang, J.; Huang, Q.; Yu, N.; Zhu, Y.; Fu, L.; Wang, F.; Chen, Y.; Wu, Y. Three-dimensional ordered porous electrode materials for electrochemical energy storage. *NPG Asia Materials* **2019**, *11*, 1-21.
8. Khan, S.A.; Ali, S.; Saeed, K.; Usman, M.; Khan, I. Advanced cathode materials and efficient electrolytes for rechargeable batteries: practical challenges and future perspectives. *J. Mater. Chem. A* **2019**, *7*, 10159-10173.
9. Buser, H.J.; Schwarzenbach, D.; Petter, W.; Ludi, A.J.I.C. The crystal structure of Prussian blue: $Fe_4[Fe(CN)_6]_3{\cdot}xH_2O$. *Inorg. Chem.*, **1977**, *16*, 2704-2710.
10. Verdaguer, M.; Girolami, G.S. Magnetic Prussian Blue Analogs. In *Magnetism: Molecules to Materials V*, Wiley, 2004; 283-346.
11. Okubo, M.; Asakura, D.; Mizuno, Y.; Kim, J.D.; Mizokawa, T.; Kudo, T.; Honma, I. Switching redox-active sites by valence tautomerism in Prussian blue analogues $A_xMn_y[Fe(CN)_6]{\cdot}nH_2O$ (A: K, Rb): Robust frameworks for reversible Li storage. *J. Phys. Chem. Lett.*, **2010**, *1*, 2063-2071.
12. Lu, Y.; Wang, L.; Cheng, J.; Goodenough, J.B. Prussian blue: a new framework of electrode materials for sodium batteries. *Chem. Commun.*, **2012**, *48*, 6544.
13. Pasta, M.; Wessells, C.D.; Huggins, R.A; Cui, Y. A high-rate and long cycle life aqueous electrolyte battery for grid-scale energy storage. *Nat. Commun.*, **2012**, *3*, 1-7.
14. Wang, B.; Han, Y.; Wang, X.; Bahlawane, N.; Pan, H.; Yan, M.; Jiang, Y. Prussian blue analogs for rechargeable batteries. *iScience*, **2018**, *3*, 110-133.
15. Hurlbutt, K.; Wheeler, S.; Capone, I.; Pasta, M. Prussian blue analogs as battery materials. *Joule*, **2018**, *2*, 1950-1960.

16. Imanishi, N.; Morikawa, T.; Kondo, J.; Yamane, R.; Takeda, Y.; Yamamoto, O.; Sakaebe, H.; Tabuchi, M. Lithium intercalation behavior of iron cyanometallates. *J. Power Sources* **1999**, *81*, 530-534.
17. Jayalakshmi, M.; Scholz, F. Performance characteristics of zinc hexacyanoferrate/Prussian blue and copper hexacyanoferrate/Prussian blue solid state secondary cells. *J. Power Sources* **2000**, *91*, 217-233.
18. Eftekhari, A. Potassium secondary cell based on Prussian blue cathode. *J. Power Sources* **2004**, *126*, 221-228.
19. Okubo, M.; Asakura, D.; Mizuno, Y.; Kudo, T.; Zhou, H.; Okazawa, A.; Kojima, N.; Ikedo, K.; Mizokawa, T.; Honma, I. Ion-Induced Transformation of Magnetism in a Bimetallic CuFe Prussian Blue Analogue. *Angew. Chemie*., **2011**, *123*, 6393-6397.
20. Wang, R.Y.; Wessells, C.D.; Huggins, R.A.; Cui, Y. Highly reversible open framework nanoscale electrodes for divalent ion batteries. *Nano Lett*., **2013**, *13*, 5748-5752.
21. Wang, L.; Lu, Y.; Liu, J.; Xu, M.; Cheng, J.; Zhang, D.; Goodenough, J.B. A superior low-cost cathode for a Na-ion battery. *Angew. Chemie*, **2013**, *52*, 2018-2021.
22. Pasta, M.; Wessells, C.D.; Liu, N et al. Full open-framework batteries for stationary energy storage. *Nat. Commun*., **2014**, *5*, 1-9.
23. Mullaliu, A.; Asenbauer, J.; Aquilanti, G.; Passerini, S.; Giorgetti, M. Highlighting the Reversible Manganese Electroactivity in Na-Rich Manganese Hexacyanoferrate Material for Li-and Na-Ion Storage. *Small Methods* **2020**, *4*, 1900529.
24. Brant, W.R.; Mogensen, R.; Colbin, S.; Ojwang, D.O.; Schmid, S.; Ha¨ggstro¨m, L.; Ericsson, T.; Jaworski, A.; Pell, A.J.; Younesi, R. Selective control of composition in Prussian white for enhanced material properties. *Chem. Mater*., **2019**, *31*, 7203-7211.
25. Asakura, D.; Li, C.H.; Mizuno, Y.; Okubo, M.; Zhou, H.; Talham, D.R. Bimetallic cyanide-bridged coordination polymers as lithium ion cathode materials: core@shell nanoparticles with enhanced cyclability. *J. Am. Chem. Soc*., **2013**, *135*, 2793-2799.
26. Mizuno, Y.; Okubo, M.; Kagesawa, K.; Asakura, D.; Kudo, T.; Zhou, H.; Oh-Ishi, K.; Okazawa, A.; Kojima, N. Precise electrochemical control of ferromagnetism in a cyanide-bridged bimetallic coordination polymer. *Inorg. Chem*., **2012**, *51*, 10311-10316.
27. Li, C.H.; Nanba, Y.; Asakura, D.; Okubo, M.; Talham, D.R. Li-ion and Na-ion insertion into size-controlled nickel hexacyanoferrate nanoparticles. *RSC Adv*., **2014**, *4*, 24955-24961.
28. Moo Lee, K.; Tanaka, H.; Ho Kim, K.; Kawamura, M.; Abe, Y.; Kawamoto. Improvement of redox reactions by miniaturizing nanoparticles of zinc Prussian blue analog. *Appl. Phys. Lett*., **2013**, *102*, 141901.
29. Fiore, M.; Wheeler, S.; Hurlbutt, K.; Capone, I.; Fawdon, J.; Ruffo, R.; Pasta, M. Paving the way toward highly efficient, high-energy potassium-ion batteries with ionic liquid electrolytes. *Chem. Mater*., **2020**, *32*, 7653-7661.
30. Li, C.H.; Peprah, M.K.; Asakura, D.; Meisel, M.W., Okubo, M.; Talham, D.R. Stepwise Reduction of Electrochemically Lithiated Core–Shell Heterostructures Based on the Prussian Blue Analogue Coordination Polymers $K_{0.1}Cu[Fe(CN)_6]_{0.7}\cdot 3.5H_2O$ and $K_{0.1}Ni[Fe(CN)_6]_{0.7\cdot 4}.4H_2O$. *Chem. Mater*., **2015**, *27*, 1524-1530.
31. Fu, H.; Liu, C.; Zhang, C.; Ma, W.; Wang, K.; Li, Z.; Lu, X.; Cao, G. Enhanced storage of sodium ions in Prussian blue cathode material through nickel doping. *J. Mater. Chem. A* **2017**, *5*, 9604-9610.
32. Tang, Y.; Zhang, W.; Xue, L.; Ding, X.; Wang, T.; Liu, X.; Liu, J.; Li, X.; Huang, Y. Polypyrrole-promoted superior cyclability and rate capability of $Na_xFe[Fe(CN)_6]$ cathodes for sodium-ion batteries. *J. Mater. Chem. A* **2016**, *4*, 6036-6041.
33. Zhang, Q.; Fu, L.; Luan, J.; Huang, X.; Tang, Y.; Xie, H.; Wang, H. Surface engineering induced core-shell Prussian blue@ polyaniline nanocubes as a high-rate and long-life sodium-ion battery cathode. *J. Power Sources* **2018**, *395*, 305-313.
34. Wang, X.; Wang, B.; Tang, Y.; Xu, B.B.; Liang, C.; Yan, M.; Jiang, Y. Manganese hexacyanoferrate reinforced by PEDOT coating towards high-rate and long-life sodium-ion battery cathode. *J. Mater. Chem. A* **2020**, *8*, 3222-3227.
35. Jiang, Y.; Yu, S.; Wang, B.; Li, Y.; Sun, W.; Lu, Y.; Yan, M.; Song, B.; Dou, S. Prussian blue@C composite as an ultrahigh-rate and long-life sodium-ion battery cathode. *Adv. Funct. Mater*., **2016**, *26*, 5315-5321.
36. Lee, C.H.; Wu, C.M.; Batsaikhan, E.; Li, H.C.; Li, C.H.; Peprah, M.K.; Talham, D.R.; Meisel, M.W.; Li, W.H. Complex Magnetic Phases in Nanosized Core@Shell Prussian Blue Analogue Cubes: $Rb_{0.48}Co[Fe(CN)_6]_{0.75}[(H_2O)_6]_{0.25}\cdot 0.34H_2O$ @$K_{0.36}Ni[Cr(CN)_6]_{0.74}[(H_2O)_6]_{0.26}\cdot 0.11H_2O$. *J. Phys. Chem. C* **2015**, *119*, 29138-29147.
37. Larson, A.C.; Von Dreele, R.B. General Structure Analysis System, Report LAUR 86-748; Los Alamos National Laboratory: Los Alamos, NM, **1994**.
38. B.E. Warren, X-ray Diffraction, Dover Publications: Dover, UK, 251, **1990**.
39. Li, W.H.; Lee, C.H. Spin polarization and small size effect in bare silver nanoparticles. In *Complex Magnetic Nanostructures*, Springer, Cham., 195-224, **2017**.